Word count: ~7500

Revision 2

Tetrahedral aluminum in tourmaline from a spinel-pargasite-metamorphosed mafic-ultramafic rock

Oleg S. Vereshchagin[1*], Yuliya D. Gritsenko[2,3], Marina F. Vigasina[3], Sergey K. Dedushenko[4], Liudmila A. Gorelova[1], Leonid A. Pautov[2,5], Atali A. Agahanov[2], Irina A. Chernyshova[1], Anatoly A. Zolotarev[1]

1 Saint Petersburg State University, University Embankment 7/9, 199034 St. Petersburg, Russia
2 Fersman Mineralogical Museum of the Russian Academy of Sciences, Leninsky Pr. 18-2, Moscow, Russia
3 Faculty of Geology, Moscow State University, Vorobievy Gory, 119991 Moscow, Russia
4 National University of Science and Technology MISIS, Leninsky Prospekt 4, 119049 Moscow, Russia
5 South Urals Federal Research Center of Mineralogy and Geoecology of the Urals Branch of the Russian Academy of Sciences, Ilmensky Reserve 1, 456317 Miass, Russia

* Corresponding author: o.vereshchagin@spbu.ru
ORCID: 0000-0002-4811-2269

ABSTRACT

Tourmaline is a widespread borosilicate mineral, which is well known for its variable chemistry. Although major amounts of octahedral Al in tourmaline is commonplace, the occurrence of significant amounts of tetrahedral Al is relatively rare. This paper focuses on tourmaline from the collection of the A.E. Fersman Mineralogical Museum (Russia) originated from Italy with up to 25% of Si replaced by Al at the tetrahedral site. The tourmaline is characterized by optical and scanning electron microscopy, Raman spectroscopy, infrared spectroscopy, Mössbauer spectroscopy, energy-dispersive and wavelength-dispersive X-ray analysis, laser ablation inductively coupled plasma optical emission spectrometry and single crystal X-ray diffraction. The studied tourmaline occurs as transparent dark blue crystals (with equant external morphology) up to 3 mm in size and forms veinlets cutting a (Mg,Al)-rich metamorphosed mafic-ultramafic rock (Mg>>Fe) composed of spinel, pargasite, clinochlore, phlogopite, and hydroxylapatite. The studied tourmaline meets the criteria defining magnesio-lucchesiite and can be compositionally formed via Tschermak-like ($^{[6]}Me^{2+}+^{[4]}\mathrm{Si}^{4+}\leftrightarrow^{[6]}\mathrm{Al}^{3+}+^{[4]}\mathrm{Al}^{3+}$, where $^{[6]}Me^{2+}$=Mg, Fe) or plagioclase-like ($^{[9]}\mathrm{Ca}^{2+} + ^{[4]}\mathrm{Al}^{3+} \leftrightarrow ^{[9]}\mathrm{Na}^{+} + ^{[4]}\mathrm{Si}^{4+}$) substitutions. Zones with a relatively high Si content (Si-rich) have pronounced indications of dissolution, while silicon-depleted zones (Si-poor) overgrow Si-rich zones and eventually creates a visible replacement zone of the crystal. We suggest that Si-poor tourmaline result from the Si-rich tourmaline losing Si during a metasomatic process. The resulting empirical crystal-chemical formula for the Si-poor zone is: $^{X}(\mathrm{Ca}_{0.95}\mathrm{Na}_{0.03}\square_{0.02})_{\Sigma1.00}$ $^{Y}(\mathrm{Mg}_{1.08}\mathrm{Al}_{0.98}\mathrm{Fe}^{2+}_{0.50}\mathrm{Fe}^{3+}_{0.43})_{\Sigma3.00}$ $^{Z}(\mathrm{Al}_{5.91}\mathrm{Fe}^{3+}_{0.09})_{\Sigma6.00}$ $^{T}[(\mathrm{Si}_{4.57}\mathrm{Al}_{1.43})_{\Sigma6.00}\mathrm{O}_{18}]$ $(\mathrm{BO}_3)_3$ $^{V}(\mathrm{OH})_3$ $^{W}[\mathrm{O}_{0.95}(\mathrm{OH})_{0.05}]_{\Sigma1.00}$ (a = 15.9811(2), c = 7.12520(10) Å, $R1$ = 1.7 %) and for the Si-rich zone is: $^{X}(\mathrm{Ca}_{0.89}\mathrm{Na}_{0.11})_{\Sigma1.00}$ $^{Y}(\mathrm{Mg}_{1.55}\mathrm{Al}_{0.80}\mathrm{Fe}^{2+}_{0.34}\mathrm{Fe}^{3+}_{0.31})_{\Sigma3.00}$ $^{Z}(\mathrm{Al}_{5.51}\mathrm{Mg}_{0.44}\mathrm{Fe}^{3+}_{0.05})_{\Sigma6.00}$ $^{T}[(\mathrm{Si}_{5.35}\mathrm{Al}_{0.65})_{\Sigma6.00}\mathrm{O}_{18}]$ $(\mathrm{BO}_3)_3$ $^{V}(\mathrm{OH})_3$ $^{\mathrm{W}}[\mathrm{O}_{0.93}(\mathrm{OH})_{0.07}]_{\Sigma1.00}$ (a=15.9621(3), c=7.14110(10) Å, $R1$=1.7 %). According to *PT* calculations of mineral assemblage stability and comparable data on synthetic $^{[4]}$Al-rich tourmalines, the studied tourmaline was formed at 600–750 °C and 0.10-0.20 GPa. The formation of tetrahedral Al-rich tourmalines requires several unusual factors: (1) desilication of primary rocks and (2) high temperatures and relatively low pressures.

Keywords: tourmaline, Tschermak substitution, tetrahedral aluminum, single-crystal X-ray diffraction, Raman spectroscopy, infrared spectroscopy, Mössbauer spectroscopy, LA ICP OES, EMPA.

INTRODUCTION

Tourmaline is a widespread borosilicate mineral (*e.g.*, Henry and Dutrow, 1996; Van Hinsberg et al. 2011; Grew et al., 2017), which could be considered as the main boron host in siliceous crustal rocks (*e.g.*, Dutrow and Henry 2011); its electrical (*e.g.*, Chernyshova et al. 2021) and optical properties (Xia and Kang 2022) make it attractive for use in material sciences. The generalized chemical formula of tourmaline supergroup minerals is $^{[9]}X^{[6]}Y_3{}^{[6]}Z_6(^{[4]}T_6O_{18})(^{[3]}BO_3)_3V_3W$, where $^{[9]}X$ = Na, K, Ca, vacancy (□),$^{[6]}Y$ = Li, Mg, Mn^{2+}, Fe^{2+}, Al, V^{3+}, Cr^{3+}, Fe^{3+}, Ti, $^{[6]}Z$ = Mg, Fe^{2+}, Al, V^{3+}, Cr^{3+}, Fe^{3+}, $^{[4]}T$ = Si, Al, B, V = O, OH, W = O, OH, F (Henry et al. 2011). These minerals are renowned for their complex crystal chemistry (*e.g.*, Bosi 2011; Vereshchagin et al. 2018; Bačík and Fridrichová 2021). To date, 40 mineral species are recognized within the supergroup, which include more than 15 species-defining elements (The official International Mineralogical Association (IMA) Commission On New Minerals, Nomenclature And Classification (CNMNC) List of Mineral Names).

The most obvious feature of tourmaline structure is the six-membered ring of [TO_4] tetrahedra, predominantly filled with silicon (*e.g.*, Bosi, 2011; Bačík and Fridrichová, 2021). Long-standing studies of natural (*e.g.*, Ertl et al. 1997; Lussier et al. 2009; Bačík et al. 2013) and synthetic tourmalines (*e.g.*, Rosenberg and Foit 1979; Ertl et al. 2015; Kutzschbach et al. 2016) showed that tetrahedral sites can be occupied by B and Al in addition to Si cations. The substitution of B for Si is mainly related to high pressures and temperatures (*PT*; *e.g.*, Kutzschbach et al. 2016; Ertl et al. 2018), while the substitution of Al for Si most likely reflects not only the changes in *PT* conditions (*e.g.*, Rosenberg and Foit 1979), but also the features of the mineral assemblage and mineral chemistry of the host rock (*e.g.*, Bačík et al. 2013).

It is important to note that despite the fact that aluminum is a ubiquitous constituent of tourmalines (*e.g.*, Henry et al. 2011), it predominantly fills octahedral sites in the crystal structure while its presence in tetrahedral sites is usually minor to insignificant ($^{[4]}$Al < 0.3 atoms per formula unit (apfu); Lussier et al. 2009). This paper focuses on (1) tourmaline from the collection of the A.E. Fersman Mineralogical Museum (Russia), which contains up to 25% of Si replaced by Al at the tetrahedral site; and (2) its relation to the formation conditions applicable to $^{[4]}$Si-poor, $^{[4]}$Al-rich tourmalines.

MATERIALS AND METHODS

The sample for this study was brought to the collection of the A.E. Fersman Mineralogical Museum (Moscow, Russia) in 1921 (record No. 10997). It was labeled as 'melanite' (Ti-bearing andradite) originating from Valtigels bei Sterzing, Tyrol, Austria-Hungary (Figure 1a), which today is known as Faltigl, Alto Adige, Italy. The sample was re-examined during the revision of museum specimens in 2020 and it turned out to be a tourmaline supergroup member.

The sample is a 5 × 6 cm fragment of dark gray fine-grained rock containing a 4 × 5 cm veinlet with tourmaline crystals (Figure 1b). The crystals were studied using optical and scanning electron microscopy (SEM), Fourier-Transform infrared spectroscopy (FTIR), Mössbauer spectroscopy (MS), Raman spectroscopy, energy-dispersive X-ray (EDS) spectroscopy and wavelength-dispersive X-ray spectroscopy (WDS), laser ablation inductively coupled plasma optical emission spectrometry (LA-ICP-OES) and single crystal X-ray diffraction (SCXRD).

The chemical composition of the crystals was analyzed on an epoxy-mounted, polished, and carbon-coated sample with the Superprobe 733 (JEOL, Japan) electron microprobe (WDS mode; 20 kV, beam current of 25 nA, 10 μm beam diameter at the sample surface) and a S–3400 N (Hitachi, Japan) scanning electron microscope equipped with an AzTec Energy XMax 20 (Oxford, UK) spectrometer (EDS mode; 20 kV, beam current of 1 nA, 1 μm beam diameter at the sample surface). A series of natural and synthetic standards were employed. The content of B, Be and Li in the tourmaline was determined using LA-ICP-OES with a VARIAN 725 spectrometer (Agilent, USA).

The empirical formula of tourmaline was calculated on the basis of 15 (T + Y + Z) atoms per formula unit (apfu) considering that: (1) vacancies may occur at the X-site, (2) there was no excess of boron (B = 3 apfu, see below). H_2O was calculated based on the electroneutral formula: ^{V}OH=3 and ^{W}O/OH ratio, based on $Y + Z + T = 15$ and MS data. Fragments of a zoned tourmaline crystal with low and high Si content (No 1 and 2; Figure 1c; Table 1) were used for Raman spectroscopy and subsequent SCXRD analysis (1-AD23 and 2-AD23, respectively).

SCXRD analysis was performed using a XtaLAB Synergy-S (Rigaku Oxford Diffraction, Japan) diffractometer equipped with a HyPix-6000HE detector operated with monochromated Mo*K*a radiation at 50 kV and 40 mA. More than a hemisphere of three-dimensional data was collected (Table 2; Crystallographic Information Files). The data were integrated and corrected for background, Lorentz, and polarization effects. The empirical absorption correction based on spherical harmonics implemented in the SCALE3 ABSPACK algorithm was applied in CrysAlisPro program (Agilent 2012). The SHELXL program package (Sheldrick 2015) was used for all structural calculations. The starting coordinates were taken from Vereshchagin et al. (2021). Site populations at the X, B, T, O(3) (=V) and O(1) (= W) sites follow the standard site preference suggested for tourmaline (*e.g.*, Henry et al. 2011). The cation assignment at the X and T sites follows the results of chemical analysis (Table 1) and bond-length considerations (in case of the T site, Ertl et al. 2018). The occupancy of the Y site was obtained considering the presence of Mg and Fe, and the occupancy of the Z site taking into account the presence of Al and Fe. The B and anion sites were modelled with B and O scattering factors, respectively, and with a fixed occupancy of 1, since the refinement with unconstrained occupancies showed no significant deviations from this value.

Raman spectra were collected using a LabRam HR 800 (Horiba Jobin-Yvon, Japan) spectrometer equipped with a BX-41 (Olympus, Japan) microscope in backscattering geometry system at ambient conditions using a 532 nm laser. The confocal hole was 100 μm, and a 1800 gr/mm grating was used. The Raman spectra of the unoriented sample were recorded in the range of 70–4000 cm^{-1} at a resolution of 2 cm^{-1} and an acquisition time of 100 s. The laser power was focused to the point of a size of ~2 μm^2 by a 100× objective. To improve the signal-to-noise ratio, the number of acquisitions was set to 5.

FTIR was performed using a FSM-1201 spectrometer (Russia) in the transmittance mode at room temperature in air over the range of wavenumbers from 400 to 4000 cm^{-1} with an accuracy of ± 2 cm^{-1}. The sample was prepared as a suspension of 5 mg of mineral powder in vaseline oil and was placed on a plane-parallel KBr plate. The IR spectrum of the same plate without suspension was used as a reference.

Room-temperature absorption Mössbauer spectra were recorded on a MS-1101 spectrometer (Russia) in the constant acceleration mode using a standard ^{57}Co source in a metallic rhodium matrix with an activity of about 2 mCi (RITVERC JSC, Russia). Isomer shifts are related to α-iron. The absorber consisted of about 10 mg powdered tourmaline crystals with the addition of sugar powder (used to ensure random crystallite orientation and increase the total volume of the sample). The resultant sample thickness was about ~0.01 mg $^{57}Fe/cm^2$. The preliminary collection of the spectrum on a larger velocity scale (between –12 and +12 mm s^{-1}) does not allow us to detect magnetic interactions. Since the impact of magnetic splitting was not detected, the spectrum was re-collected between –5 and +5 mm s^{-1} to improve resolution. The spectrum was fitted using the HappySloth software (http://happysloth.ru/).

RESULTS

Mineral assemblage and tourmaline optical properties

Tourmaline forms veinlets cutting a (Mg,Al)-rich rock composed of spinel (spinel-hercynite solid solution, Mg:Fe ~2:1), pargasite (Mg:Fe ~3:1), clinochlore (Mg:Fe ~8:1), phlogopite (Mg:Fe

~8:1), and hydroxylapatite. In addition, allanite-(Ce) containing Ln_2O_3 ~ 12-15 wt. %, (Ln = La, Ce, Nd) and zircon were found as inclusions within the tourmaline in question.

Tourmaline occurs as short prismatic to equant crystals up to 3 mm in size (Figure 1a-d). The crystals are transparent, with vitreous luster; brittle, with irregular fracture. The color of tourmaline is dark deep blue, with a white streak. In thin section, it is strongly pleochroic from dark deep blue to grey. It is uniaxial (–), refraction indices measured in Si-poor zone (for more details see below) are: $\omega = 1.666(2)$, $\varepsilon = 1.642(2)$ (589 nm).

Chemical composition

All tourmaline crystals under study are chemically zoned (a typical zone size 20-200 μm; Fig. 1). The main tetrahedral cation is Si (4.57-5.47 apfu; Table 1). Zones with relatively high Si content (Si-rich) have pronounced textures consistent with dissolution (Figure 1c-d). In contrast, a silicon-depleted zone (Si-poor) overgrows the Si-rich zones and crosscuts the crystal.

The tourmaline belongs to the calcic group (Ca 0.83-0.95 apfu; Table 1) and oxy-subgroup (O 0.72-0.95 apfu). The maximum aluminum content in the tetrahedral site reaches 25% and no tetrahedral boron is present (according to LA-ICP-OES, FTIR, Raman spectroscopy and SCXRD (see below)). Aluminum is also the main octahedral cation (6.22-6.91 apfu) and is present in both Y- and Z-sites as its content is always higher than 6 apfu. All zones being investigated are Mg-rich (Mg 1.06-2.08 apfu) and Fe-bearing (Fe_{total} 0.55-1.02 apfu). The content of Li and Be was found to be negligible (<0.1 wt.%). No excess of boron was found by LA-ICP-OES and it was assumed to be stoichiometric (3.00 B apfu) in accordance with the results of FTIR, Raman spectroscopy and SCXRD. This is consistent with the previous studies indicating that $^{[4]}B$ is consistently absent in Mg-rich tourmalines (Lussier et al. 2009).

The studied tourmaline meets the criteria defining magnesio-lucchesiite as follows: Ca is dominant at the X-site, Mg is dominant at the Y-site, Al is dominant at the Z-site, O is dominant at the *W*-site. It is worth noting that both octahedral and tetrahedral Al is not species defining in magnesio-lucchesiite and should be ignored (Henry et al. 2011; Scribner et al. 2021). It is interesting to note that the studied tourmaline (magnesio-lucchesiite) contains a significant amounts (up to ~33 %) of a hypothetical $CaAl_3Al_6(Si_3Al_3)O_{18}(BO_3)_3(OH)_3O$ end member, the content of which is almost equal to the content of magnesio-lucchesiite.

Raman spectroscopy

Raman spectra were obtained from the two zones: Si- rich (No. 2, Fig. 1c) and Si- poor (No. 1, Fig. 1c). The spectrum obtained from the Si-rich zone (Fig. 2b) has the best resolution compared to the spectrum obtained from the Si-poor sample zone (Fig. 2a). However, the main characteristic Raman bands corresponding to internal vibrations of the structural elements are present in both spectra. It is worth noting that the tourmaline spectrum (Fig. 2b) obtained in the Si-rich zone of the sample (Fig. 1c, point 2) is consistent with that of synthetic oxy-uvite and adachiite (Berryman et al. 2016a; Watenphul et al. 2016, respectively) .

Deformation vibrations of [TO_4] rings are attributed to the lines at 224, 246, 277, 378 cm^{-1} and symmetrical stretching vibrations of [TO_4] rings correspond to the line at 490 cm^{-1} (Watenphul et al. 2016). The scattering line at 341 cm^{-1} belongs to the low-frequency bending mode of O-*T*-O in tetrahedral (Watenphul et al. 2016). The scattering line at 564 cm^{-1} corresponds to the highest frequency bending mode of O-*T*-O in tetrahedra [TO_4] (Watenphul et al. 2016). The lines at 715 and 757 cm^{-1} can be attributed to symmetric stretching vibrations of $[BO_3]^{3-}$ anions (Watenphul et al. 2016). Lines at 663 and 987 cm^{-1} are attributed to antisymmetric stretching vibrations of *T*-O bonds in six-membered rings (Watenphul et al. 2016). The scattering line with two components at 1058 and 1110 cm^{-1} corresponds to symmetric and antisymmetric stretching vibrations of *T*-O bonds in [TO_4] groups (Watenphul et al. 2016). A line with low intensity at 1325 cm^{-1} is attributed to antisymmetric stretching vibrations of $[BO_3]^{3-}$ anions (Watenphul et al. 2016). The absence of lines in the spectral range 3300-3430 cm^{-1} indicates the absence of boron in the tetrahedral position (Kutzschbach et al. 2021). The asymmetric intense band in the range of 3400 - 3590 cm^{-1} corresponds to stretching vibrations of O-H groups at the *V*-site (Peng et al. 1989; Watenphul et al. 2016).

Infrared spectroscopy

A relatively small size of compositional zones made it impossible to collect infrared spectra from the Si-rich and Si-poor zones separately. Only the total spectrum was obtained (Figure 3). The FTIR spectrum of the tourmaline in hand (Fig. 3) is consistent with that of adachiite and magnesio-lucchesiite (Nishio-Hamane et al. 2014; Scribner et al. 2021, respectively).

The bands corresponding to stretching vibrations of six-membered rings $[(Si,Al)O_4]_6$, bending vibrations of $[(Si,Al)O_4]$ and of $[BO_3]$ groups and lattice modes were observed in the spectral range 400 – 850 cm^{-1}. In this range, the spectra of both samples are practically identical both in shape and in the values of absorption band maxima. In the spectral region 800 – 1200 cm^{-1}, spectrum (II) exhibits weakly resolved absorption bands. A band with a maximum at 1281 cm^{-1} and a very weak shoulder at 1315 cm^{-1} correspond to stretching vibrations of $[BO_3]$-groups, a slightly split band at 982-1026 cm^{-1} can be attributed to stretching vibrations of $[(Si,Al)O_4]$-groups.

In the spectrum of sample (I), similar absorption bands are clearly resolved into a larger number of components. Thus, the absorption band related to stretching vibrations of $[(Si,Al)O_4]$-groups is split into three components 977, 1028 and 1074, cm^{-1} and the absorption band of $[BO_3]$-groups has three components with absorption maxima at 1245, 1291 and 1351 cm^{-1}. A two-component band observed in the range 3300–3650 cm^{-1} is attributed to stretching vibrations of OH-groups. A high-frequency component with weak intensity near 3628 cm^{-1} should be attributed to hydroxyl groups at the *W*-site (Nishio-Hamane et al. 2014).

Mössbauer spectroscopy

The relatively small size of the zones did not allow to collect spectra from the Si-rich and Si-poor zones separately. Only the total spectrum was obtained (Figure 4). The Mössbauer spectrum of the tourmaline under study consists of broadened lines of different intensity and can be described by the superposition of two symmetrical doublets (Fe^{3+}: $^{RT}IS_{\alpha\text{-}Fe}$ 0.41(7), ^{RT}QS 0.88(14) mm s^{-1}; Fe^{2+}: $^{RT}IS_{\alpha\text{-}Fe}$ 1.03(8), ^{RT}QS 2.06(15) mm s^{-1}). Along with components (doublets) with isomer shifts typical of [$Fe^{3+}O_6$], it contains components with isomer shifts close to 1.0 mm s^{-1}, which are commonly attributed to [$Fe^{2+}O_6$] (*e.g.,* Bačík et al. 2013; Scribner et al. 2021). At the same time, this isomer shift is completely atypical of divalent iron in octahedral coordination with oxygen (*e.g.*, Menil 1985). The relative areas of the doublets are similar (~48 and 52 % for Fe^{2+} and Fe^{3+}, respectively), which indicates that Fe^{2+}: Fe^{3+} ratio is ~1:1. It should be noted that the complication of the spectrum fitting model with the isolation of several different doublets of di- or trivalent iron with close isomer shifts and different quadrupole splitting does not mean that the corresponding iron atoms are at different crystallographic sites. Indeed, the differences in the local environment of iron atoms, which may exist in the sample, may affect the QS value (Dedushenko and Perfiliev 2022).

Crystallography

The tourmalines being under investigation are characterized by minor variations in the unit cell parameters (Table 2). An interesting feature of 1AD-23 is a low ratio of unit cell parameters (*c/a* 0.446), which is one of the lowest among tourmalines (Fig. 5a).

X-site scatterings (Crystallographic Information file; Supplementary Table S1-S2) indicate that the XO_9 polyhedron in both cases (samples 1AD-23 and 2AD-23) is almost completely occupied by calcium, which is in a good agreement with the chemical composition (0.95 and 0.89 apfu, respectively; Table 1). The <*X*-O> distances for samples 1AD-23 and 2AD-23 (2.633 and 2.632 Å, respectively; Table 3) practically coincide with an analogous distance in the structure of magnesio-lucchesiite (2.626 Å), whose *X* site has a similar composition ($Ca_{0.88}Na_{0.12}$; Scribner et al. 2021; Tables 1, 3).

Y- and *Z*–site scatterings (Supplementary Table S1-S2) and bond-lengths (Table 3) indicate that the YO_6 octahedron in both cases (samples 1AD-23 and 2AD-23) is mainly filled with magnesium and aluminum (Mg>Al), while the ZO_6 octahedron is mainly filled with aluminum (see below). All divalent iron was assumed to be present at the *Y*-site only in accordance with the previous studies (e.g., Bačík et al., 2013; Nishio-Hamane et al., 2014), while trivalent iron fills both non-equivalent octahedral sites (mainly YO_6). The <*Y*-O> distances for samples 1AD-23 and 2AD-23 (2.025 and 2.021 Å, respectively) are significantly higher than the <*Y*-O> distance in synthetic ^{Y,Z}Al-rich tourmaline (<^{Y}Al-O>=1.928 Å; Marler et al., 2002). This indicates the presence of large cations (Mg and Fe; Table 1) at the YO_6 octahedron as $^{[6]}Al^{3+} < ^{[6]}Fe^{3+} < ^{[6]}Mg^{2+} < ^{[6]}Fe^{2+}$ (0.535 < 0.645< 0.72 < 0.78 Å; Shannon, 1976). The <*Z*-O> distances for samples 1AD-23 and 2AD-23 (1.916 and 1.920 Å, respectively) are close but slightly higher than the <*Z*-O> distance in synthetic ^{Y,Z}Al-rich tourmaline (<^{Z}Al-O>=1.914 Å; Marler et al., 2002). This is a sign of the presence of large cations at the Z-site.

The <*T*-O> distances for samples 1AD-23 and 2AD-23 (1.645 and 1.639 Å, respectively) are significantly higher than the <*T*-O> distance in $^{[4]}$Al-free tourmaline (<^{T}Si-O>=1.622 Å; Scribner et al., 2021) and represent the highest known values within the tourmaline supergroup. Interestingly, the <*T*-O> distances for samples 1AD-23 are even higher than in the structure of Ge-rich tourmaline (<*T*-O>=1.640 Å; Setkova et al. 2023), which also indicates unusually low contents of tetrahedral silicon $^{[4]}Ge \approx ^{[4]}Al > ^{[4]}Si$ (0.39 > 0.39 > 0.26 Å; Shannon, 1976). The <*T*-O> distances for samples 1AD-23 and 2AD-23 (Fig. 5b) are also much higher than those in the crystal structure of adachiite (1.634 Å; Nishio-Hamane et al. 2014) and magnesio-lucchesiite (1.634 Å, Scribner et al. 2021).

The occurrence of (OH) groups only at the O(3) site and mixed (O,OH) at O(1) site was proposed based on EDX, MS and examination of bond-valence sums (Supplementary Table S3-4). Bond valence sums on O1 site is ~ 1.5, indicating O>OH. Bond valence sums on O3 site is ~ 1, indicating OH only.

The resulting empirical crystal-chemical formula for 1AD-23 is: $^{X}(Ca_{0.95}Na_{0.03}\square_{0.02})_{\Sigma=1.00}$ $^{Y}(Mg_{1.08}Al_{0.98}Fe^{2+}_{0.50}Fe^{3+}_{0.43})_{\Sigma=3.00}$ $^{Z}(Al_{5.91}Fe^{3+}_{0.09})_{\Sigma=6.00}$ $^{T}[(Si_{4.57}Al_{1.43})_{\Sigma=6.00}O_{18}]$ $(BO_3)_3$ $^{V}(OH)_3$ $^{W}[O_{0.95}(OH)_{0.05}]_{\Sigma=1.00}$ and for 2AD-23 is: $^{X}(Ca_{0.89}Na_{0.11})_{\Sigma=1.00}$ $^{Y}(Mg_{1.55}Al_{0.80}Fe^{2+}_{0.34}Fe^{3+}_{0.31})_{\Sigma=3.00}$ $^{Z}(Al_{5.51}Mg_{0.44}Fe^{3+}_{0.05})_{\Sigma=6.00}$ $^{T}[(Si_{5.35}Al_{0.65})_{\Sigma=6.00}O_{18}]$ $(BO_3)_3$ $^{V}(OH)_3$ $^{W}[O_{0.93}(OH)_{0.07}]_{\Sigma=1.00}$.

DISCUSSION

All zones of the studied tourmaline can be compositionally formed via Tschermak-like substitution ($^{[6]}Me^{2+}+^{[4]}Si^{4+} \leftrightarrow {}^{[6]}Al^{3+}+^{[4]}Al^{3+}$, where $^{[6]}Me^{2+}$=Mg, Fe; Fig. 6a). The tourmaline in question has a rather high and constant content of calcium (0.83-0.95 apfu; Table 1), however another substitution may be playing an important role in $^{[4]}$Al-enriched tourmalines: $^{[9]}Ca^{2+} + {}^{[4]}Al^{3+} \leftrightarrow {}^{[9]}Na^{+} + {}^{[4]}Si^{4+}$ (plagioclase-like or paragonite / margarite-like; Fig. 6b). Both substitutions are possible and further research is required to show which of the mechanisms is more often (more fully) implemented in tourmaline supergroup minerals.

It was previously shown that the addition of an Al_2O_3 component to a simple MgO–SiO_2–H_2O system results in a pressure–temperature dependency of Tschermak substitution in antigorite; it was also demonstrated that $^{[4]}$Al in serpentine can be used to constrain metamorphic conditions (Padrón-Navarta et al. 2013). In general, the operation of this type of substitution to enhance $^{[4]}$Al will be favored by an increasing temperature and bulk compositions that are aluminous and, to a lesser extent, silica poor (*e.g.*, Pattison 1987; Padrón-Navarta et al. 2013).

The studied tourmaline is characterized by the presence of complex zoning, in which the Si-rich zones (Si > 5 apfu) are always highly dissolved (have uneven boundaries; Figure 1c, d).

Simultaneously, the silicon-depleted zones (Si ~4.5-5.0 apfu) are the outer zones of the crystal (Figure 1c, d). We can assume the removal of silicon from the early generation of tourmaline (Si-rich zones) and the formation of the second, later generation (Si-poor) with simultaneous recrystallization. It is worth noting both adachiite (Nishio-Hamane et al. 2014) and the studied tourmaline have strong zonation. Possible desilication process is also indirectly confirmed by the absence of quartz (this study; Nishio-Hamane et al. 2014; Scribner et al. 2021). This dissolution and replacement phenomenon of two generations of tourmaline was also described by Henry et al. (2002, 2003).

The studied tourmaline was found in spinel-pargasite-clinochlore rocks. Previously, the formation conditions for spinel + pargasite were calculated as 0.2 GPa and 650–750 °C based on pseudosections and simplified phase diagrams of the system (Nozaka et al. 2016). These *PT* parameters seem to be reasonable for the studied tourmaline, since synthetic $^{[4]}$Al-enriched tourmaline in association with spinel and pargasite was obtained under comparable conditions (see below).

Both garnet and tourmaline have been mentioned since the beginning of 19th century in various metamorphic rocks from Valtigels bei Sterzing, Italy (e.g., von Senger, 1821; Doblicka, 1852). However, the exact location of the find raises questions, since tourmaline is quite common in this part of Tyrol (e.g., mindat.org) and the area is characterized by relatively high-grade metamorphism (e.g., Zanchetta et al., 2023), which is not fully consistent with the studied rock. Simultaneously, the specimen studied bears a resemblance to the tourmaline from the Elba island, Italy (Dottorini, 2020). To date, it is not possible to accurately answer the question of the origin of the sample from the Fersman Mineralogical Museum with absolute certainty. Therefore, we suggest treating the question of its origin with some caution.

Tourmalines with high amounts of $^{[4]}$Al (> 0.5 apfu) are rarely found in nature. According to Lussier et al. (2009), there is no clear correspondence between the species of tourmaline and $^{[4]}$Al content. Ertl et al. (2018) suggested that relatively high amounts of $^{[4]}$Al may be expected in Mg- and/or Fe^{2+}-rich tourmalines, especially when they are of aluminous bulk compositions and have experienced high temperature metamorphic conditions.

Indeed, all natural $^{[4]}$Al-rich tourmalines are Al- and Mg- and/or Fe^{2+}-rich. The studied tourmaline is the most $^{[4]}$Al-rich (up to 1.43 apfu; Table 1) species in the tourmaline supergroup known so far. Previously, the highest $^{[4]}$Al value (0.95 apfu) was reported in another Ca-, Mg-rich tourmaline (magnesio-lucchesiite; $CaMg_3Al_6(Si_6O_{18})(BO_3)_3(OH)_3O$), which was found in hydrothermal veins embedded in meta-serpentinites within the contact aureole of the Monte Capanne intrusion, Elba Island, Italy (Scribner et al. 2021). Ca, Fe-rich tourmaline (adachiite; $CaFe_3Al_6(Si_5AlO_{18})$ $(BO_3)_3(OH)_3(OH)$) ranks third in $^{[4]}$Al content (0.84 apfu) and was found in a hydrothermal vein, crosscutting a lateritic metamorphic rock (mainly consisting of corundum and hercynite) near Saiki City, Oita Prefecture, Japan (Nishio-Hamane et al. 2014). Another example worth mentioning is Na, Fe-rich tourmaline (oxy-schorl; $Na(Fe^{2+}_2Al)Al_6(Si_6O_{18})(BO_3)_3(OH)_3O$) with significant amount of $^{[4]}$Al (0.49 apfu), it was found in fracture fillings cutting altered metarhyolite pyroclasts near Zlatá Idka village, Slovak Ore Mountains, Slovak Republic (Bačík et al. 2013). Besides, Na-, Fe-, $^{[4]}$Al- enriched tourmaline of the schorl - dravite - ferridravite series with relatively high $^{[4]}$Al content (up to 0.42 apfu) were reported from Larderello Geothermal Field, Italy (Cavarretta and Puxeddu, 1990).

All synthetic $^{[4]}$Al-rich tourmalines are Al-enriched (Al_{total}> 6 apfu) and contain significant amounts of magnesium or copper. The highest $^{[4]}$Al content (up to 1.78 apfu) was reported in Na, Al-rich (0.94, 9.0 apfu, respectively) tourmaline synthesized at 600 ˚C and 0.1 GPa (Rosenberg et al. 1986). However, single-crystal refinement, which could confirm $^{[4]}$Al content, has not been done.

Besides, synthesis conditions and unit cell parameters (close to synthetic olenite; Marler et al., 2002) indicate that the tetrahedral aluminum content may be overestimated, while the tetrahedral boron content may be underestimated. Lebedev et al. (1998) synthesized a tourmaline containing 0.56 Na, 1.74 Mg and 8.34 Al, including 1.08 tetrahedral Al (per formula unit), at 600 ˚C and 0.15 GPa aluminum (no single-crystal refinement data were provided). Moreover, several of Fe-Mg tourmalines synthesized by Lebedev et al. (1988) are associated with spinel, pargasite and Mg-rich mica group mineral. Consequently, we suggest that the formation conditions for the studied tourmaline could be like those of the syntheses, that is, 600-750 ˚C and 0.1-0.2 GPa. The next largest $^{[4]}$Al content (up to 0.90 apfu) was found in Cu-rich tourmaline synthesized at 600 ˚C and 0.15 GPa (Lebedev et al. 1988; Vereshchagin et al. 2013; Ertl et al. 2015). $^{[4]}$Al content was proved by single-crystal refinement. Berryman et al. (2015) reported a series of $^{[4]}$Al-rich tourmalines (0.54-0.75 apfu), which were synthesized at a temperature range 500-700 ˚C and pressure 0.4-3 GPa (no single-crystal refinement data were provided). All of them are Mg-, Al-rich (Mg>2.17, Al>6.55 apfu) and most of them (5 out of 6 reported compositions) were obtained at high pressure (3 GPa). These tourmalines belong either to Na-dominant or to *X*-site vacant species (Berryman et al. 2015). Berryman et al. (2016b) reported another $^{[4]}$Al-rich tourmaline (0.59 apfu), which was synthesized at 500 ˚C and 1 GPa. This tourmaline belongs to the *X*-site vacant (0.54 apfu) group and is a Mg-, Al-rich (Mg 2.17, Al 6.83 apfu) specie (no single-crystal refinement data were provided). Interestingly, the studies of synthetic tourmalines have shown a weak, but significant correlation of the Tschermak substitution with the pressure of synthesis: $^{[4]}$Al decreases with increasing pressure (Krosse, 1995; Werding, and Schreyer, 1996).

It should be noted that most synthetic Al- and Mg- and/or Fe^{2+}-rich tourmalines and natural tourmalines contain negligible amounts of tetrahedral aluminum (*e.g.*, Lebedev et al. 1988; Berryman et al. 2015, 2016b). This may be due to (1) the sequence of phase crystallization (earlier phases deplete the solution in silicon), (2) the effect of pressure (as they were obtained at pressure 0.15-3 GPa). It is necessary for tourmaline to be undersaturated with silicon so that a significant amount of tetrahedral aluminum appears. Most likely, such conditions can be realized if the silicon content in the system decreases due to the crystallization of the associated phases or desilication (see above).

IMPLICATIONS

According to the modern classification, tourmalines are borosilicates (Henry et al. 2011), since [TO_4] tetrahedra are filled with silicon only in most cases. Previous studies show that in some cases tourmalines can be considered as boro-aluminosilicates, since up to 25% of silicon can be replaced by aluminum in tetrahedra.

Our data, together with those previously published on adachiite (Nishio-Hamane et al. 2014), indicate that the high content of aluminum in the tetrahedral site is achieved due to Si removal by the primary generations of tourmaline. Thus, tourmaline enriched in tetrahedral aluminum can be an indicator of metasomatic transformation of rocks. The possibility of the formation of primary tourmaline depleted in silicon seems unlikely, since multiple syntheses of tourmaline in an aluminum-rich medium led to the formation of tourmalines enriched in $^{[4]}$B, but not $^{[4]}$Al (*e.g.*, Kutzschbach et al. 2016). However, at present there is too little data to establish this accurately. One can conclude that the formation of such boro-aluminosilicate tourmalines is a rather rare process and is apparently associated with several factors: (1) desilication of primary rocks and (2) high temperatures and relatively low pressures process.

We suggest that experiments on the dissolution-recrystallization of tourmalines in silicon-depleted solutions can help answer this question. In addition, in the future such studies will help to more accurately use tourmalines to assess the conditions necessary for its formation.

ACKNOWLEDGMENTS

The authors thank X-ray Diffraction Centre and Geomodel Center of Resource Centre of Saint Petersburg State University for providing instrumental and computational resources. We are thankful to the Associate Editor, Edward Grew, and two reviewers, Aaron Lussier and Darrell Henry, who contributed significantly to improving the quality of the manuscript. This research was funded by Council for Grants of the President of the Russian Federation NSH-1462.2022.1.5 (for OSV, LAG and IAC).

REFERENCES

Agilent (2012) CrysAlis PRO. Agilent Technologies, Oxfordshire, UK.

Bačík, P., and Fridrichová, J. (2021) Cation partitioning among crystallographic sites based on bond-length constraints in tourmaline-supergroup minerals. American Mineralogist, 106, 851–861.

Bačík, P., Cempírek, J., Uher, P., Novák, M., Ozdín, D., Filip, J., Škoda, R., Breiter, K., Klementová, M., Ďuďa, R., and others (2013) Oxy-schorl, $Na(Fe_2Al)Al_6Si_6O_{18}(BO_3)_3(OH)_3O$, a new mineral from Zlatá Idka, Slovak Republic and Přibyslavice, Czech Republic. American Mineralogist, 98, 485–492.

Berryman, E.J., Wunder, B., Wirth, R., Rhede, D., Schettler, G., Franz, G., and Heinrich, W. (2015) An experimental study on K and Na incorporation in dravitic tourmaline and insight into the origin of diamondiferous tourmaline from the Kokchetav Massif, Kazakhstan. Contributions to Mineralogy and Petrology, 169, 1–16.

Berryman, E. J., Wunder, B., Ertl, A., Koch-Müller, M., Rhede, D., Scheidl, K., Giester, G., and Heinrich, W. (2016a) Influence of the X-site composition on tourmaline's crystal structure: investigation of synthetic K-dravite, dravite, oxy-uvite, and magnesio-foitite using SREF and Raman spectroscopy. Physics and Chemistry of Minerals, 43, 2, 83-102.

Berryman, E.J., Wunder, B., Rhede, D., Schettler, G., Franz, G., and Heinrich, W. (2016b) P–T–X controls on Ca and Na distribution between Mg–Al tourmaline and fluid. Contributions to Mineralogy and Petrology, 171, 1–31.

Bosi, F. (2011) Stereochemical constraints in tourmaline: From a short-range to a long-range structure. Canadian Mineralogist, 49, 17–27.

Cavarretta, G. and Puxeddu, M. (1990) Schorl - dravite - ferridravite tourmalines deposited by hydrothermal magmatic fluids during early evolution of the Larderello Geothermal Field, Italy. Economic Geology, Vol. 85, 1236-1251.

Chernyshova, I.A., Vereshchagin, O.S., Malyshkina, O. V, Goncharov, A.G., Kasatkin, I.A., Murashko, M.N., Zolotarev, A.A., and Frank-Kamenetskaya, O. V (2021) Tourmalines pyroelectric effect depending on the chemical composition and cation oxidation state. Journal of Solid State Chemistry, 303, 122512.

Dedushenko, S.K., and Perfiliev, Y.D. (2022) On the correlation of the 57Fe Mössbauer isomer shift and some structural parameters of a substance. Hyperfine Interactions, 243, 1–25.

Doblicka, K. (1852) Tirols Mineralien, 138 pages (in German)

Dottorini, V. (2020) Cristallochimica di specie del supergruppo della tormalina dalla Toscana. Master thesis, University Pisa, 284 pages.

Dutrow, B., and Henry, D. (2011) Tourmaline: a geologic DVD. Elements, 7, 301–306.

Ertl, A., Pertlik, F., and Bernhardt, H.-J. (1997) Investigations on Olenite with Excess Boron from the Koralpe, Styria, Austria. Österr. Akad. Wiss., Math.-naturwiss. Kl. Abt. I, Anzeiger, 3–10.

Ertl, A., Vereshchagin, O.S., Giester, G., Tillmanns, E., Meyer, H.P., Ludwig, T., Rozhdestvenskaya, I. V., and Frank-Kamenetskaya, O. V. (2015) Structural and chemical investigation of a zoned synthetic Cu-rich tourmaline. Canadian Mineralogist, 53, 209–220.

Ertl, A., Henry, D.J., and Tillmanns, E. (2018) Tetrahedral substitutions in tourmaline: a review. European Journal of Mineralogy, 30, 465–470.

Grew, E. S., Hystad, G., Hazen, R.M., Krivovichev, S.V. and Gorelova, L. A. (2017) How many boron minerals occur in Earth's upper crust? American Mineralogist, 102, 8, 1573–1587.

Henry, D.J. and Dutrow, B.L. (1996) Metamorphic tourmaline and its petrologic applications. In Boron: Mineralogy, Petrology and Geochemistry (E.S. Grew & L.M. Anovitz, eds.). Mineralogical Society of America, Reviews in Mineralogy 33, 503–557.

Henry, D. J., Dutrow, B. L. and Selverstone, J. (2002) Compositional polarity in replacement tourmaline – an example from the Tauern Window, Eastern Alps. Geological Materials Research, 4, no. 2, 23 p

Henry, D. J., Dutrow, B. L. and Selverstone, J. (2003) Compositional polarity in replacement tourmaline – an example from the Tauern Window, Eastern Alps. American Mineralogist, 88, 1399.

Henry, D.J., Novák, M., Hawthorne, F.C., Ertl, A., Dutrow, B.L., Uher, P., and Pezzotta, F. (2011) Nomenclature of the tourmaline-supergroup minerals. American Mineralogist, 96, 895–913.

Krosse S (1995) Hochdrucksynthese, Stabilität und Eigenschaften der Boisilikate Dravit und Komerupin sowie Darstellung und Stabilitätsverhalten eines neuen Mg-Al-borates. Unpublished Doctor's thesis Ruhr-Universität, Bochum.

Kutzschbach, M., Wunder, B., Rhede, D., Koch-Müller, M., Ertl, A., Giester, G., Heinrich, W., and Franz, G. (2016) Tetrahedral boron in natural and synthetic HP / UHP tourmaline: Evidence from Raman spectroscopy, EMPA, and single-crystal XRD. American Mineralogist, 101, 93–104.

Kutzschbach, M., Wunder, B., Wannhoff, I., Wilke, F.D.H., Couffignal, F., and Rocholl, A. (2021) Raman spectroscopic quantification of tetrahedral boron in synthetic aluminum-rich tourmaline. American Mineralogist, 106, 872–882.

Lebedev, A.S., Kargalcev, S.V., and Pavlychenko, V.. (1988) Synthesis and properties of tourmaline series Al-Mg-(Na) and Al-Fe-(Na). In Genetic and Experimental Mineralogy. Growth and Properties of Crystals pp. 58–75. Novosibirsk (in Russian).

Lussier, A.J., Aguiar, P.M., Michaelis, V.K., Kroeker, S., and Hawthorne, F.C. (2009) The occurrence of tetrahedrally coordinated al and b in tourmaline: An ^{11}B and ^{27}Al MAS NMR study. American Mineralogist, 94, 785–792.

Marler, B., Borowski, M., Wodara, U. and Schreyer, W. (2002) Synthetic tourmaline (olenite) with excess boron replacing silicon in the tetrahedral site: II. Structure analysis. European Journal of Mineralogy, 14, p. 763 - 771.

Menil, F. (1985) Systematic trends of the ^{57}Fe Mössbauer isomer shifts in (FeOn) and (FeFn) polyhedra. Evidence of a new correlation between the isomer shift and the inductive effect of the competing bond T-X (→ Fe) (where X is O or F and T any element with a formal positive charge). Journal of Physics and Chemistry of Solids, 46, 763–789.

Nishio-Hamane, D., Minakawa, T., Yamaura, J., Oyama, T., Ohnishi, M., and Shimobayashi, N. (2014) Adachiite, a Si – poor member of the tourmaline supergroup from the Kiura mine, Oita Prefecture, Japan. Journal of Mineralogical and Petrological Sciences, 109, 74–78.

Nozaka, T., Meyer, R., Wintsch, R.P., and Wathen, B. (2016) Hydrothermal spinel, corundum and diaspore in lower oceanic crustal troctolites from the Hess Deep Rift. Contributions to Mineralogy and Petrology, 171, 1–14.

Padrón-Navarta, J.A., Sánchez-Vizcaíno, V.L., Hermann, J., Connolly, J.A.D., Garrido, C.J., Gómez-Pugnaire, M.T., and Marchesi, C. (2013) Tschermak's substitution in antigorite and consequences for phase relations and water liberation in high-grade serpentinites. Lithos, 178, 186–196.

Pattison, D.R.M. (1987) Variations in Mg/(Mg+Fe), F, and (Fe,Mg)Si = 2Al in pelitic minerals in the Ballachulish thermal aureole, Scotland. American Mineralogist, 72, 255–272.

Peng, M., Ma, H., Chen, L., and Chao, E.C.T. (1989) The polarized Raman spectra of tourmaline. Annual report of the Director Geophysical Laboratory, 99–105.

Rosenberg, P.E., and Foit, F.F. (1979) Synthesis and characterization of alkali-free tourmaline. American Mineralogist, 64, 180–186.

Rosenberg, P.E., Foit, F.F., Jr., and Ekambaram, V. (1986) Synthesis and characterization of tourmaline in the system Na_2O-Al_2O_3-SiO_2-B_2O_3-H_2O. American Mineralogist, 71, 97l-976.

Shannon, R.D. (1976) Revised effective ionic radii and systematic studies of interatomic distances in halides and chalcogenides. Acta Crystallographica, 32, 751–767.

Scribner, E.D., Cempírek, J., Groat, L.A., Evans, R.J., Biagioni, C., Bosi, F., Dini, A., Hålenius, U., Orlandi, P., and Pasero, M. (2021) Magnesio-lucchesiite, $CaMg_3Al_6(Si_6O_{18})(BO_3)_3(OH)_3O$, a new species of the tourmaline supergroup. American Mineralogist, 106, 862–871.

Setkova, T. V., Borovikova, E.Y., Zarubina, E.S., Anosova, O.A., Aksenov, S.M., Frolov, K. V., Balitsky, V.S., Bublikova, T.M., and Pushcharovsky, D.Y. (2023) Crystal Growth and Complex Characterization of Novel Gallium- and Germanium-Rich Tourmalines: Refinement of the Crystal Structure, Cation Distribution, and Raman and Mössbauer Spectroscopy. Crystal Growth and Design, (in press).

Sheldrick, G.M. (2015) Crystal structure refinement with SHELXL. Acta Crystallographica, C71, 3–8.

Van Hinsberg, V.J., Henry, D.J., and Marschall, H.R. (2011) Tourmaline: An ideal indicator of its host environment. Canadian Mineralogist, 49, 1–16.

Vereshchagin, O.S., Rozhdestvenskaya, I. V., Frank-Kamenetskaya, O. V., Zolotarev, A.A., and Mashkovtsev, R.I. (2013) Crystal chemistry of Cu-bearing tourmalines. American Mineralogist, 98, 1610–1616.

Vereshchagin, O.S., Frank-Kamenetskaya, O. V., Rozhdestvenskaya, I. V., and Zolotarev, A.A. (2018) Incorporation of 3d elements in tourmalines: structural adjustments and stability. European Journal of Mineralogy, 30, 917–928.

Vereshchagin, O.S., Britvin, S.N., Wunder, B., Frank-Kamenetskay, O.V., Wilke, F.D.H., Vlasenko, N.S., Shilovskikh, V.V., Bocharov, V.N., Danilov, D.V. (2021) Ln^{3+} (Ln^{3+} = La, Nd, Eu, Yb) incorporation in synthetic tourmaline analogues: Towards tourmaline REE pattern explanation. Chemical Geology, 584, 120526.

von Senger, W.E. (1821) Versuch einer Oryctographie der gefürsteten Grafschaft Tirol, 110 pages (in German)

Watenphul, A., Burgdorf, M., Schlüter, J., Horn, I., Malcherek, T., and Mihailova, B. (2016) Exploring the potential of Raman spectroscopy for crystallochemical analyses of complex hydrous silicates: II. Tourmalines. American Mineralogist, 101, 970–985.

Werding, G. and Schreyer, W. (1996), Experimental studies on borosilicates and selected borates. Mineralogical Society of America, Reviews in Mineralogy, 33, 117-163.

Xia, M., and Kang, L. (2022) Tourmaline with ultraviolet optical nonlinearity: Emergent material discovery from mineral. Journal of Alloys and Compounds, 892, 162235.

Zanchetta, S., Cucato M., Bove, G., Morelli, C., Poli, S. and Zanchi A. (2023) Note Illustrative della carta Geologica d'Italia in scala 1:50.000, foglio 006 "San Leonardo in Passiria". Servizio Geologico d'Italia - ISPRA, 328 pp.

Table 1. Chemical composition (wt.%) and atomic proportion in the chemical formula of the studied tourmaline and some related species.

		This work							Nishio-Hamane et al., 2014	Scribner et al., 2021		Bačík et al., 2013
		1AD-23	2AD-23	1	2	3	4	5		Italy	Canada	Zlatá Idka
SiO_2		27.35	31.93	27.43	27.82	29.96	31.06	32.73	34.71	30.26	35.23	33.10
Al_2O_3		42.33	35.22	42.97	40.15	40.67	37.07	34.22	34.36	39.30	26.63	39.81
TiO_2		bdl	bdl	0.00	0.00	0.00	0.02	0.14	0.00	bdl	1.92	0.02
MgO		4.26	7.97	5.58	5.59	6.74	7.52	8.33	9.16	5.82	7.96	2.31
FeO		3.60	2.37	2.55	3.22	2.14	2.58	2.60	1.34	2.90	4.34	7.97
Fe_2O_3		4.11	2.85	2.61	3.37	2.10	2.67	2.57	1.27	2.86	6.14	bdl
Cr_2O_3		bdl	bdl	bdl	bdl	bdl	bdl	bdl	bdl	bdl	0.10	bdl
V_2O_3		bdl	bdl	bdl	bdl	bdl	bdl	bdl	bdl	bdl	0.08	bdl
Na_2O		0.10	0.33	0.31	0.38	0.47	0.46	0.33	1.16	0.37	1.19	1.83
K_2O		bdl	bdl	bdl	bdl	bdl	bdl	bdl	bdl	bdl	0.04	bdl
CaO		5.32	4.98	5.10	5.06	4.78	4.68	4.98	3.05	4.93	3.27	0.58
F		bdl	bdl	bdl	bdl	bdl	bdl	bdl	bdl	0.04	0.41	0.26
H_2O_{calc}		2.73	2.75	2.96	2.84	2.91	2.91	2.74	2.96	2.60	2.29	2.92
B_2O_{3calc}		10.39	10.36	10.48	10.28	10.58	10.44	10.39	10.54	10.41	10.23	10.45
-O=F										0.02	0.17	0.11
Total		100.20	98.76	99.99	98.70	100.35	99.42	99.03	98.55	99.47	99.67	99.18
(Y+Z+T)=15 atoms per formulae unit (apfu)												
X	Ca	**0.95**	**0.89**	**0.91**	**0.92**	**0.84**	**0.83**	**0.89**	**0.62**	**0.88**	**0.60**	0.10
	Na	0.03	0.11	0.10	0.12	0.15	0.15	0.11	0.28	0.12	0.39	**0.59**
	K	-	-	-	-	-	-	-	-	-	0.01	0.30
	□	0.02	0.00	0.00	0.00	0.01	0.02	0.00	0.10	0.00	0.00	-
Y* + *Z	Al	**6.91**	**6.31**	**6.94**	**6.71**	**6.80**	**6.44**	**6.22**	**6.63**	**6.79**	**5.31**	**7.31**
	Mg	1.06	1.99	1.38	1.40	1.65	1.87	2.08	0.60	1.45	2.02	0.57
	Fe^{2+}	0.50	0.33	0.35	0.46	0.29	0.36	0.36	1.72	0.40	0.62	1.11
	Fe^{3+}	0.52	0.36	0.33	0.43	0.26	0.33	0.32	-	0.46	0.79	-
	Ti	-	-	0.00	0.00	0.00	0.00	0.02	0.06	-	0.25	-
	Cr	-	-	-	-	-	-	-	-	-	0.01	-
	V	-	-	-	-	-	-	-	-	-	0.01	-
	Total	9.00	9.00	9.00	9.00	9.00	9.00	9.00	9.01	9.00	9.01	9.00
T	Si	**4.57**	**5.35**	**4.55**	**4.70**	**4.92**	**5.17**	**5.47**	**5.15**	**5.05**	**5.98**	**5.51**
	Al	1.43	0.65	1.45	1.30	1.08	0.83	0.53	0.85	0.95	0.02	0.49
	Total	6.00	6.00	6.00	6.00	6.00	6.00	6.00	6.00	6.00	6.00	6.00
V	O	3.00	3.00	3.00	3.00	3.00	3.00	3.00	3.00	2.90	2.59	3.00
	OH	-	-	-	-	-	-	-	-	0.10	0.41	-
	Total	3.00	3.00	3.00	3.00	3.00	3.00	3.00	3.00	3.00	3.00	3.00
W	O	**0.95**	**0.93**	**0.72**	**0.80**	**0.81**	**0.76**	**0.94**	0.44	**0.98**	**0.78**	**0.63**
	OH	0.05	0.07	0.28	0.20	0.19	0.24	0.06	**0.56**	-	-	0.23
	F	-	-	-	-	-	-	-	-	0.02	0.22	0.14
	Total	1.00	1.00	1.00	1.00	1.00	1.00	1.00	1.00	1.00	1.00	1.00

Note: * - numbers are those from Figure 1, bdl – below detection limit. 1AD-23 and 2AD-23 are data for crystals used for SCXRD.

Table 2. Crystal parameters, data collection and structure refinement details for the studied tourmaline and some related species

Crystal data	This work		Nishio-Hamane et al., 2014	Scribner et al., 2021		Bačík et al., 2013
	1AD-23	2AD-23		Italy	Canada	Zlatá Idka
Crystal system, space group	Trigonal, *R*3*m*					
a (Å)	15.9811(2)	15.9621(3)	15.9290(2)	15.9270(10)	15.9910(3)	15.916(3)
c (Å)	7.12520(10)	7.14110(10)	7.1830(1)	7.1270(5)	7.2224(2)	7.1071(12)
V ($Å^3$)	1575.94(5)	1575.71(6)	1578.39(4)	1565.7(2)	1599.42(7)	1559.1(4)
Z	3					
Data collection and refinement						
Diffractometer	Rigaku XtaLAB Synergy-S		Bruker SMART CCD	Bruker X8 APEX II		Oxford Diffraction KM-4 Xcalibur
Radiation	Mo Kα					
No. of measured, independent and observed [$I > 2\sigma(I)$] reflections	10149, 1588, 1557	11511, 1392, 1385	5589, 1886	9398, 1273, 1225	21660, 3214, 2953	3174, 1474, 1111
R_{int}, R_σ	0.029, 0.016	0.035, 0.017	0.040	0.050, 0.033	0.042, 0.033	
$2\Theta_{max}$ (°)	71	68	80	63	91	72
R_1, wR_2,	0.017, 0.047	0.017, 0.045	0.038, 0.093	0.019, 0.042	0.031, 0.056	0.034, 0.066
S	1.101	1.119	1.09	1.07	1.052	0.84
$\Delta\rho_{max}$, $\Delta\rho_{min}$ (e $Å^{-3}$)	0.57, -0.35	0.46, -0.35	1.19, -0.80	0.31, -0.44	1.10, -1.10	0.67, -0.38

Table 3. Bond lengths (Å) in main polyhedrons and polyhedral volumes (Å^3) of the studied tourmaline in comparison with published data

	This study		Nishio-Hamane et al., 2014	Scribner et al., 2021		Bačík et al., 2013
	1AD-23	2AD-23		Italy	Canada	Zlatá Idka
X - O2 [3x]	2.542(2)	2.525(2)	2.556	2.526(3)	2.4799(19)	2.561(4)
- O4 [3x]	2.639(2)	2.642(2)	2.736	2.718(3)	2.7774(18)	2.710(3)
- O5 [3x]	2.718 (2)	2.730(2)	2.667	2.635(3)	2.6971(18)	2.781(3)
Mean	2.633	2.632	2.653	2.626	2.652	2.684
Y - O1(*W*) [1x]	1.949(2)	1.941(2)	1.989	1.930(2)	2.0112(19)	1.944(3)
- O2 [2x]	2.038(1)	2.036(2)	2.028	2.0255(19)	2.0455(12)	1.981(2)
- O3*V* [1x]	2.188(2)	2.175(2)	2.204	2.156(3)	2.175(2)	2.132(3)
- O6 [2x]	1.967(1)	1.969(2)	2.003	1.9554(19)	2.0270(12)	1.965(2)
Mean	2.025	2.021	2.043	2.008	2.055	1.995
Z - O3(*V*) [1x]	1.996(1)	1.995(1)	1.978	1.8838(18)	1.9871(9)	1.9890(15)
- O6 [1x]	1.870(1)	1.878(2)	1.867	1.9007(18)	1.8953(12)	1.869(2)
- O7 [1x]	1.876(1)	1.885(1)	1.941	1.8858(18)	1.9728(12)	1.876(2)
- O7 [1x]	1.926(1)	1.936(1)	1.883	1.9223(19)	1.9728(12)	1.925(2)
- O8 [1x]	1.903(1)	1.903(1)	1.895	1.9325(18)	1.9027(12)	1.889(2)
- O8 [1x]	1.927(1)	1.925(1)	1.930	1.9943(13)	1.9346(13)	1.918(2)
Mean	1.916	1.920	1.916	1.920	1.933	1.911
T - O4 [1x]	1.665(1)	1.662(1)	1.633	1.625(2)	1.6328(7)	1.6412(15)
- O5 [1x]	1.646(1)	1.642(1)	1.653	1.6160(18)	1.6496(8)	1.6298(12)
- O6 [1x]	1.639(1)	1.630(2)	1.630	1.6389(11)	1.6019(12)	1.633(2)
- O7 [1x]	1.630(1)	1.621(1)	1.619	1.6584(13)	1.6034(11)	1.625(2)
Mean	1.645	1.639	1.634	1.634	1.622	1.632
B - O2 [1x]	1.391(3)	1.387(3)	1.378	1.372(3)	1.380(3)	1.380(6)
- O8 [2x]	1.373(2)	1.374(2)	1.369	1.383(5)	1.3754(16)	1.373(3)
Mean	1.379	1.378	1.372	1.376	1.377	1.375

Note: the numbers in square brackets correspond to frequency of bonds.

Figure 1. The studied tourmaline: (a) crystals (black) in bedrock (with label), (b) equant crystals, (c) dissolved Si-rich zones (dark) inside Si-poor crystal (BSE-image), (d) Si-rich zone inside Si-poor crystal (BSE-image). Number are as in Table 1 and Figure 2

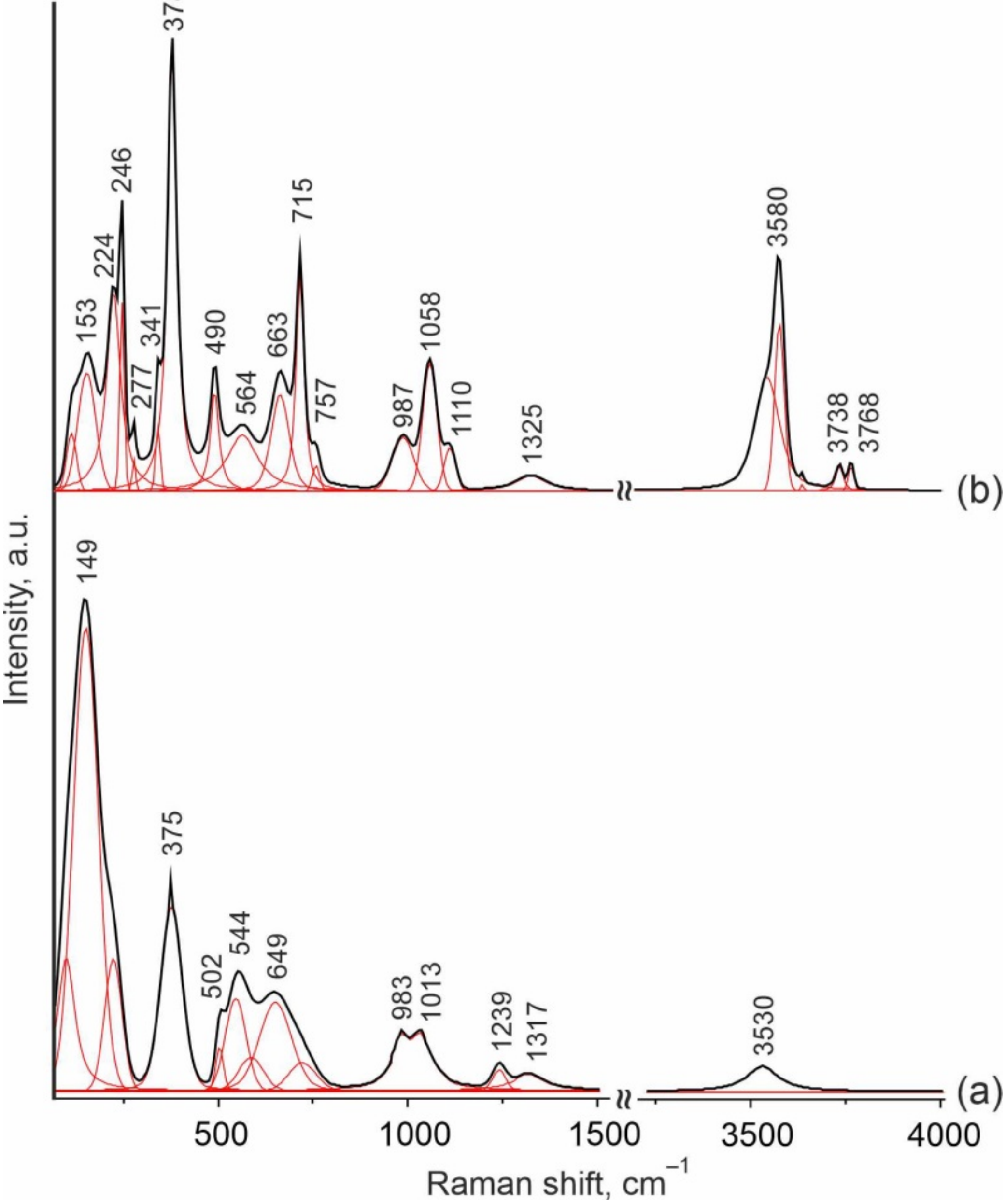

Figure 2. The Raman spectra of the studied tourmaline: (a) – Si-poor zone (No 1; Figure 1), (b) – Si-rich zone (No 2; Figure 1). The black line shows the experimental data, red line — peak deconvolution.

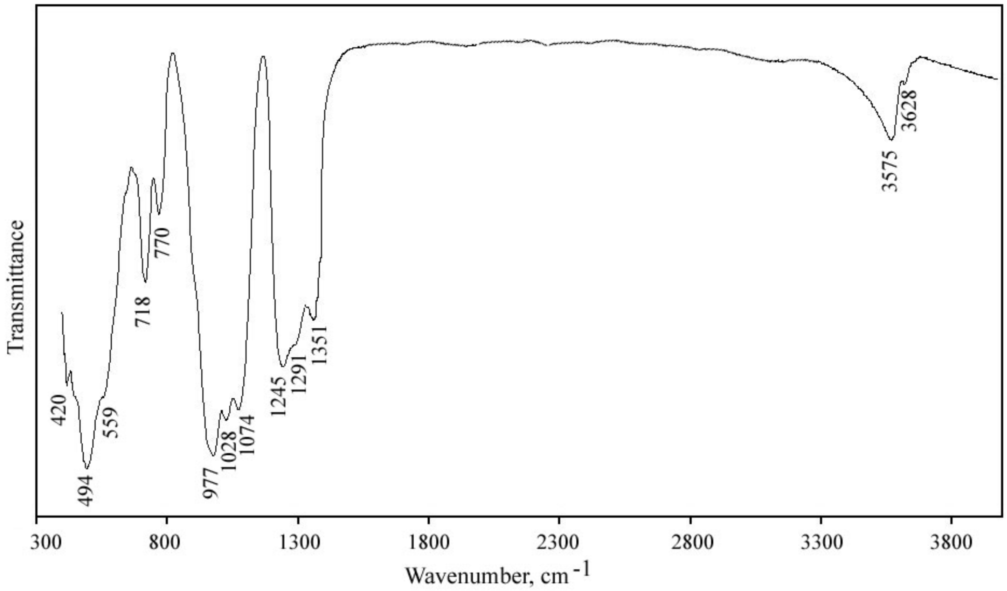

Figure 3. Powder infrared absorption spectrum of the studied tourmaline.

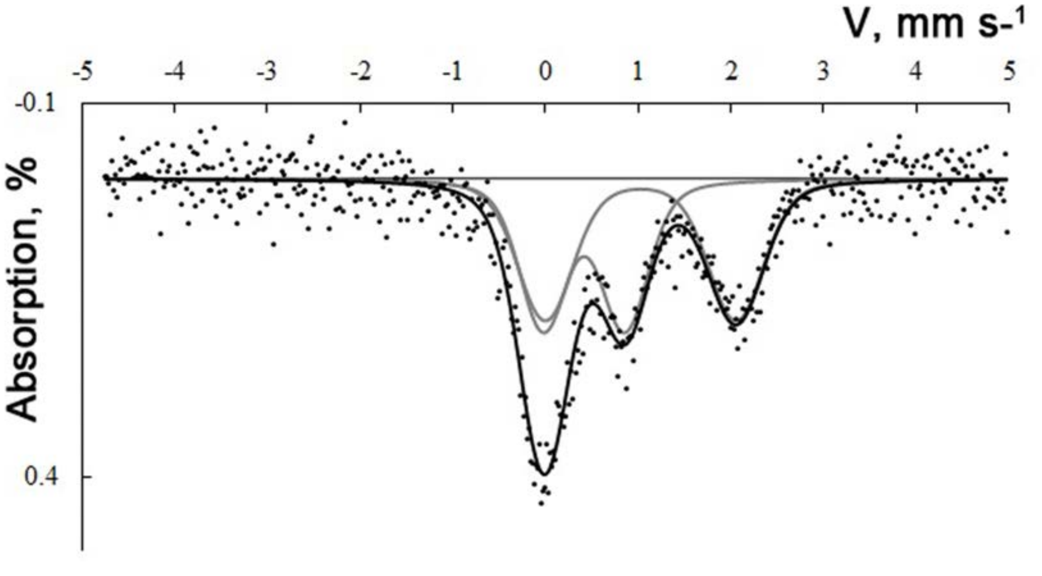

Figure 4. Room-temperature Mössbauer spectrum of the studied tourmaline.

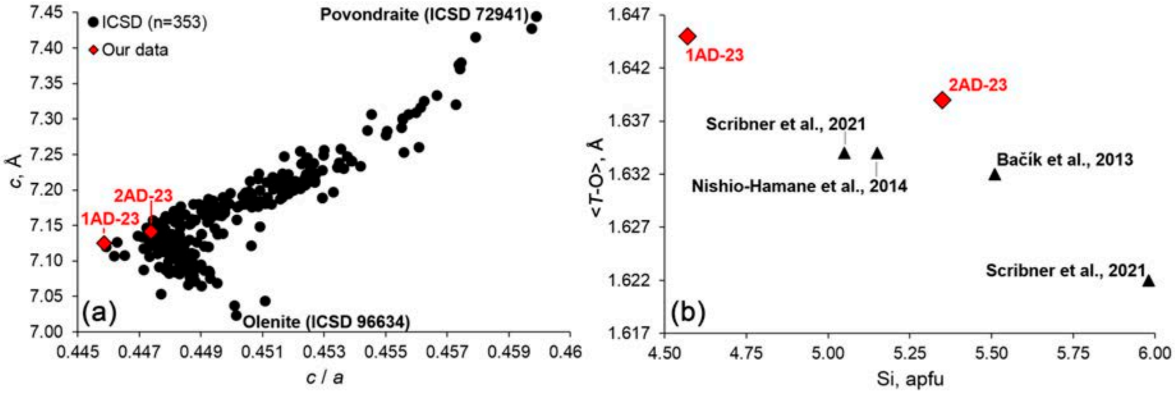

Figure 5. Crystallographic data on the studied tourmaline in comparison with published data: (a) – *c* unit cell parameter *vs*. *c* / *a* ratio, (b) – <*T*-O> distance *vs.* Si apfu. Note ICSD - Inorganic Crystal Structure Database (accessed 05.08.2023)

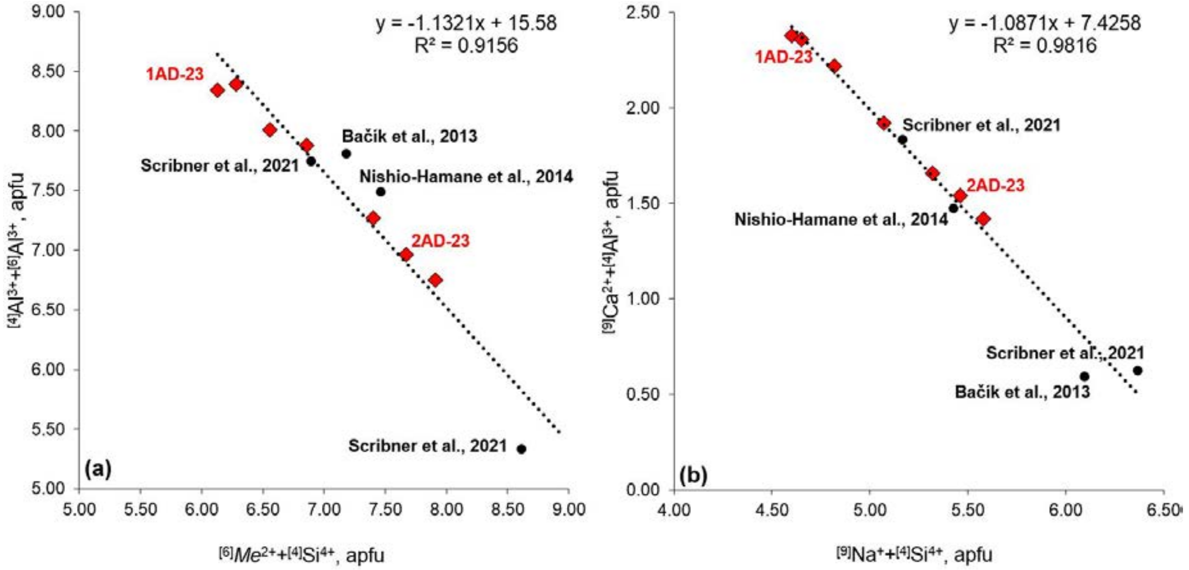

Figure 6. Chemical composition data on the studied tourmaline in comparison with published data: (a) – $^{[6]}Al^{3+}+^{[4]}Al^{3+}$ *vs.* $^{[6]}Me^{2+}+^{[4]}Si^{4+}$, (b) – $^{[9]}Ca^{2+} + ^{[4]}Al^{3+}$ *vs.* $^{[9]}Na^{+} + ^{[4]}Si^{4+}$. Note: black circles correspond to literature data, red diamonds correspond to our data.